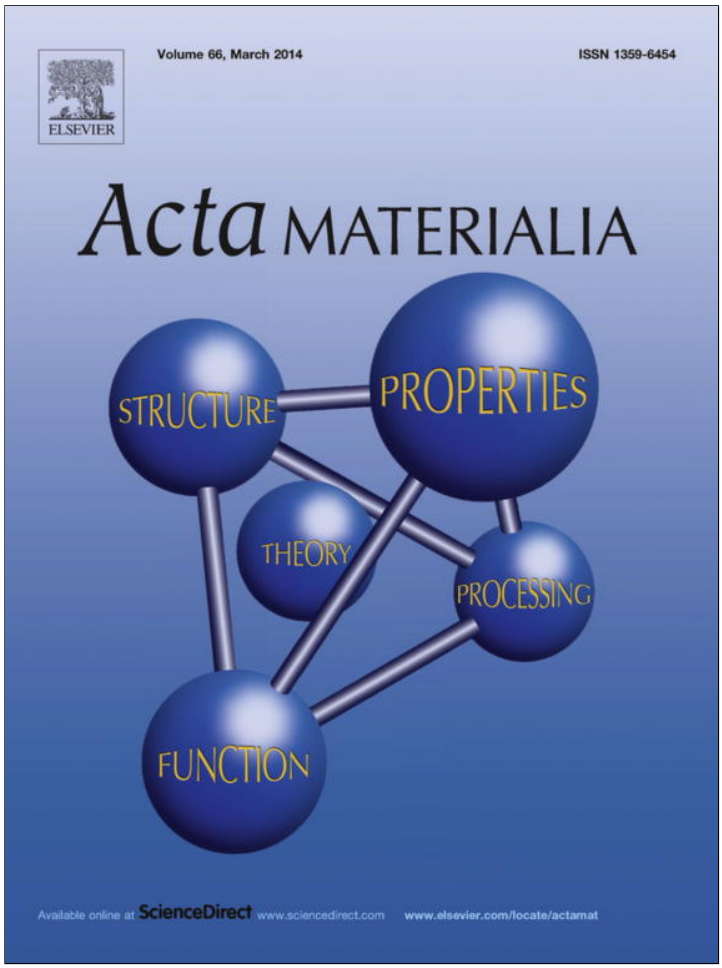

Available online at www.sciencedirect.com

ScienceDirect

Acta Materialia 66 (2014) 302–316

Acta MATERIALIA

www.elsevier.com/locate/actamat

Emergence of external size effects in the bulk-scale polycrystal to small-scale single-crystal transition: A maximum in the strength and strain-rate sensitivity of multicrystalline Cu micropillars

J.Y. Zhang, X. Liang, P. Zhang, K. Wu, G. Liu *, J. Sun *

State Key Laboratory for Mechanical Behavior of Materials, Xi'an Jiaotong University, Xi'an 710049, People's Republic of China

Received 16 April 2013; received in revised form 4 November 2013; accepted 5 November 2013
Available online 3 December 2013

Abstract

Using microcompression methodology, various plastic deformation characteristics, namely the strength, strain-rate sensitivity (SRS) and activation volume, of ⟨100⟩-single-crystalline (SC) Cu micropillars and nanostructured multicrystalline (MC) Cu micropillars with several grains were systematically investigated at different strain rates for a wide range of external sample sizes ranging from 300 to 2000 nm. The results revealed that the paradigm of "smaller is stronger" for small-scaled SC pillars holds true in nanostructured MC Cu micropillars above the strongest external size; however, below this size, a decrease in the external size triggers the reverse size effect, i.e. "smaller is weaker". The appropriate introduction of grain boundaries into SC pillars can markedly improve the smoothness of their plastic flow and significantly enhance their SRS. Additionally, we demonstrated that the SRS of MC Cu pillars increases with decreasing size up to a certain limit and then decreases with a further decrease in the external sample size; thus, a maximum SRS emerges. A phenomenological model was proposed to rationalize the scaling behavior of the activation volume with the external sample size and to highlight the effect of the internal feature size on the rate-limiting behavior of conventional bulk nanostructured metals (Cu).

Keywords: Cu micropillar; Plastic deformation; Strength; Strain-rate sensitivity; Size effect

1. Introduction

The continuing trend of miniaturizing materials for many modern technological applications has led to a strong demand for an understanding of the complex mechanical properties of materials at small length scales [1,2]. A size-scale effect can be defined as a change in the mechanical properties of metals due to a change either in the dimensions of an internal feature or structure or in the overall physical dimensions of the sample [3,4]. The development of a microcompression technique that enables the compression of pillars with diameters (ϕ) of <10 μm has opened new routes for the investigation of the mechanics of such small-scale materials [1,2,5,6]. Microcompression has revealed a "smaller is stronger" trend for single-crystalline (SC) pillars with non-zero initial dislocation densities when ϕ is reduced to <10 μm [7–18]. This trend has perplexed material scientists because it does not fit into classical crystal plasticity, according to which the strength of a single crystal depends not on its size but rather on its geometrically predicted dislocation slip system(s) with the highest resolved shear stress [13,14]. The size-driven strength (σ) in such free-surface-dominated materials is described by an empirical power law: $\sigma = A\phi^{-\alpha}$, where A is a constant and α is the power-law exponent, which ranges from 0.5 to 1 [1,2,5,6]. Currently, the micromechanisms of size-dependent strengthening for such face-centered cubic (fcc) SC materials are commonly explained by dislocation starvation [19,20], which may

* Corresponding authors. Tel.: +86 (0)2982667143; fax: +86 (0) 2982663453.
E-mail addresses: lgsammer@mail.xjtu.edu.cn (G. Liu), junsun@mail.xjtu.edu.cn (J. Sun).

1359-6454/$36.00
http://dx.doi.org/10.1016/j.actamat.2013.11.018

occur for nanometer-scale crystalsm and source truncation [21–23] or source exhaustion [24,25], which have been demonstrated on the submicron and micron scales. In addition to the size-driven strength, fcc SC pillars also exhibit other unexpected plastic characteristics, such as an intermittent and stochastic plastic flow [3,26,27] and a high strain-rate sensitivity (SRS, m) or a low activation volume (V^*) [10,28]. Recently, Jennings et al. [10] demonstrated using uniaxial deformation experiments performed at different constant strain rates ($\dot{\varepsilon}$) that SRS emerges in $\langle 1\,1\,1\rangle$-SC Cu nanopillars with diameters ranging from 75 to 500 nm. In the ranges of pillar diameters and strain rates tested, the authors found that the transition diameter was a function of the strain rate, i.e. faster strain rates shifted the transition diameter to smaller pillar diameters [10]. In pillars with diameters greater than the transition diameter, dislocations nucleate from Frank–Read-type bulk sources. Below the transition diameter, dislocations nucleate from the surface [10].

Unlike small-scale fcc SC metals, the plastic characteristics in conventional bulk-scale polycrystalline (PC) materials are dominated by internal grain boundaries (GBs). These GBs hinder the motion of gliding dislocations and thus provide effective barriers to the transmission of dislocations from one grain to another. The strength of PC metals increases with decreasing grain size (d), as described by the well-known Hall–Petch equation [29]. However, when d is below a critical value (~15–20 nm), the dominant deformation mechanism transforms from dislocation-mediated to GB-mediated (GB sliding and grain rotation) activities; thus, a softening behavior (i.e. the so-called "inverse Hall–Petch relation" [30]) is expected in nanocrystalline (NC) materials [31]. Bulk-scale nanostructured PC materials, such as Cu [32–33], Ni [34–35] and Au [36], exhibit an increased SRS m (and a smaller V^*) compared with their coarse-grained counterparts, similarly to small-scale SC nanopillars [10,28]. The increasing SRS with decreasing characteristic size that was observed in bulk-scale fcc PC materials has been quantified by various theoretical models [32,35,37]. It is well accepted that the deformation of fcc materials from the dislocation motion that is produced by the activation of bulk sources (Frank–Read sources or single-arm sources) usually induces a lower SRS (and a larger V^* of $\sim 100b^3$–$1000b^3$), whereas the deformation that is due to dislocation nucleation from GBs induces a higher SRS (and a smaller V^* of $\sim 1b^3$–$10b^3$) [10,29,38]. Therefore, a large difference in V^* should be manifested in the vastly different $\dot{\varepsilon}$ dependences between the two mechanisms, and GB sources should be more sensitive to $\dot{\varepsilon}$ than bulk sources.

As evidence of these unique behaviors emerges in either small-scale SC materials or bulk-scale nanostructured PC materials, a crucial question naturally arises: how do external sample size reduction effects influence the plastic characteristics of metals with a fixed internal structure or feature size? To distinguish different sample conditions, it is tempting to assign a parameter, i.e. the external-to-internal size ratio (η), that equals 1 for SC materials ($\eta = \phi/d = 1$), e.g. various small-scale SC pillars [7–18], and ∞ for conventional PC materials, e.g. bulk-scale nanostructured metals [32–35]. At intermediate length scales (e.g. $3 \leqslant \eta \leqslant 20$) between nanosized SC pillars and nanostructured PC metals, the strength of multicrystalline (MC) nanostructures has been reported to increase [39,40] or decrease [41,42]. It is particularly important to understand the yield strength of nanostructured MC materials as a function of the sample dimensions at the regime where the internal (microstructure) and external (sample dimension) length scales compete. Specifically, using 3D-DDD simulations, Csikor et al. [27] noted that MC pillars exhibited an appreciable smoothing of deformation compared with SC pillars because the strain burst that is caused by internal dislocation avalanches can be limited by the existence of GBs. However, the role that internal homogeneous GBs play in the burst behavior is still unclear, and the effect of internal GBs on the plastic characteristics, such as the flow strength, SRS and activation volume, of these small-scale MC pillars is worth studying in order to understand their deformation mechanism(s). Additionally, in terms of a fundamental understanding of plasticity, the (coupling) effects of the internal feature size and the external sample dimension on the plastic deformation is an issue of scientific importance.

In this paper, we systematically investigate the SRS of MC Cu pillars that contain several grains with a diameter ($\phi \approx 300$–2000 nm)-to-grain size ($d \approx 110$–180 nm) ratio η of ~3–20 and the SRS of SC Cu pillars with diameters (ϕ) ranging from 300 to 1200 nm at different strain rates to fully understand the influence of GBs on the deformation of MC pillars at the micron and submicron scales. We clearly reveal that the MC micropillars exhibit external size reduction effects on the flow strength and SRS, i.e. the maximum strength and SRS emerge at a critical η. Furthermore, we demonstrate that the problem of intermittent and stochastic strain burst behavior can be alleviated through the introduction of GBs into SC pillars and that a more stable hardening can be achieved, resulting in a higher strength.

2. Experimental procedures

2.1. Cu film synthesis and microstructural characterization

At room temperature, two types of Cu thin films were prepared on a HF-etched $\langle 1\,0\,0\rangle$-Si substrate through direct current magnetron sputtering using different deposition rates. One type is ~1.6 μm thick Cu films with nanometer- and submicron-sized grains, which were deposited on the Si substrate at ~0.8 nm s^{-1}. The other type is ~2 μm thick Cu films with micron-sized grains, which were deposited on the Si substrate at ~0.5 nm s^{-1}. The chamber was evacuated to a base pressure of $\sim 6.0 \times 10^{-8}$ torr prior to sputtering, and a pressure of $\sim 2.0 \times 10^{-3}$ torr Ar was used during the deposition process. X-ray diffraction (XRD) experiments were conducted using an improved Rigaku D/max-RB

X-ray diffractometer with Cu Kα radiation and a graphite monochromator to determine the crystallographic texture. Transmission electron microscopy (TEM) observations were performed using a JEOL-2100 high-resolution (HR) electron microscope with a 200 kV accelerating voltage to observe the microstructural features of the Cu films.

2.2. Fabrication of Cu micropillars

MC Cu micropillars with $\phi = 340$–1200 nm and SC Cu micropillars with $\phi = 300$–1200 nm were fabricated from the Cu thin films using the focused ion beam (FIB) technique in a Helios 600 Dual Beam instrument, which is also capable of scanning electron microscopy (SEM) imaging. The Cu pillar preparation process consisted of two steps and followed the approach adopted by Greer et al. [43]. To minimize the potential damage from ion irradiation due to the Ga ion beam and to clean any newly deposited materials from the pillar surface, the final FIB fine milling step was performed under a reduced voltage (15 kV) and current (15 pA). More details can be found in our previous works [44,45]. The height-to-diameter ratios (i.e. aspect ratios) of the "pure" Cu pillars are between ~1.7 and ~7 for the SC pillars and between ~1 and ~6 for the MC pillars. In the range of ~2–7, the effects of the aspect ratio on the deformation behavior of the Cu pillars are weak, particularly for the MC Cu pillars. This has been detailed in Ref. [46] and will not be discussed in the present work. The taper angles (ψ) of the pillars are between 2° and 4°.

It should be noted that, due to the limited thicknesses of the as-deposited Cu thin films, only the top of the machined pillars is composed of Cu, and the base consists of the substrate material (Si). Compared to other nanopillars made from bulk, which usually have a trench at their bottom, our pillars have a clearly visible interface with the Si substrate, which ensures an accurate measurement of sample dimensions. Furthermore, dislocations cannot penetrate beneath the pillars since the substrate consists of a very hard and stiff material, Si. The deformation of the Si portion of the sample is purely elastic, so accurate measurements of the plastic displacement of Cu pillars are feasible by subtracting the elastic displacements of Cu and Si from the total displacement of the whole structure. For these reasons, the calculations of stress–strain curves are more accurate than those of pillars made from bulk crystals [47,48].

2.3. Flat-punch compression test

Microcompression tests were performed on a Hysitron Ti 950 using a 10 μm flat punch and a quadrilateral cross-section diamond indenter. The tip–pillar alignment was performed using an optical microscope. All of the micropillars were compressed under rate-controlled mode at a strain rate ($\dot{\varepsilon}$) ranging from 2×10^{-4} to $2 \times 10^{-2}\ s^{-1}$ up to a ~30% strain, followed by a holding segment of 5 s prior to unloading. The force–displacement data were continuously recorded, and the engineering stress–strain curves were then calculated using the initial geometry of the pillar, which was determined from the SEM images. The cross-sectional area at the half height of the pillar (A_0) and the initial height (L_0) were used for the calculations. Based on our previous works [44,45], an attempt was made to correct for the compliance of the base of the (Si) pillar by using the model of a perfectly rigid, circular, flat punch indented onto an isotropic half space, which was first proposed by Sneddon [49]. To improve the reliability and accuracy of the present measurements, efforts were devoted to the correction of thermal drift in the microcompression test. In the present study, the allowable drift rate was $0.01\ nm\ s^{-1}$, which is 10-fold smaller than the value ($0.1\ nm\ s^{-1}$) generally used in typical nanoindentation/micropillar compression tests. If the drift rate exceeded $0.01\ nm\ s^{-1}$, the experimental data were discarded. Therefore, in the present test, the effect of thermal drift could be minimized and neglected. True stress–strain curves were used to characterize the deformation behavior [43,47,50]. After taking into account the substrate effect and the taper correction, the true strain ε_T and the true stress σ_T can be simply expressed as:

$$\varepsilon_T = \frac{1}{E_{Cu}}\frac{PL_p}{A_0L_0} + \ln\left(\frac{L_0}{L_p}\right) = \frac{1+\frac{L_0}{r_0}\tan\psi}{E_{measured}}\frac{PL_p}{A_0L_0} + \ln\left(\frac{L_0}{L_p}\right) \quad (1)$$

and

$$\sigma_T = \frac{P}{A_p} = \frac{PL_p}{A_0L_0} = \frac{P}{A_0L_0}\left\{L_0 - \left[u_{tot} - \frac{\sqrt{\pi}P(1-\nu^2)}{2E_{Si}\sqrt{A_{Si}}}\right]\right\}, \quad (2)$$

where A_0 is the cross-sectional area at the half initial height (L_0) of the pillar, r_0 is the radius at the top of the pillar, L_p is the final height, A_p is the average cross-sectional area, P is the load, E_{Cu} is the true modulus of the Cu pillars without tapers, $E_{measured}$ is the measured modulus of the tapered Cu pillars, u_{tot} is the total displacement, ν is Poisson's ratio of Cu (~0.343), and A_{Si} and E_{Si} are the average cross-sectional area and modulus of the substrate Si pillar, respectively. Note that the influence of the taper (ψ) has been taken into account in the above equations.

3. Experimental results

3.1. Microstructure of the SC/MC Cu pillars

The XRD results revealed that the 2 μm thick Cu films exhibited a quasi-SC microstructure with a strong (100) texture, from which SC Cu pillars with a ⟨100⟩ orientation were fabricated through FIB. In contrast, the 1.6 μm thick Cu thin films exhibited polycrystalline nanostructured features with random orientations. The cross-sectional TEM micrograph of the ~2 μm thick Cu thin films revealed relatively high densities of dislocations at the top and bottom of the ⟨100⟩-SC Cu micropillars, as clearly shown in Fig. 1a

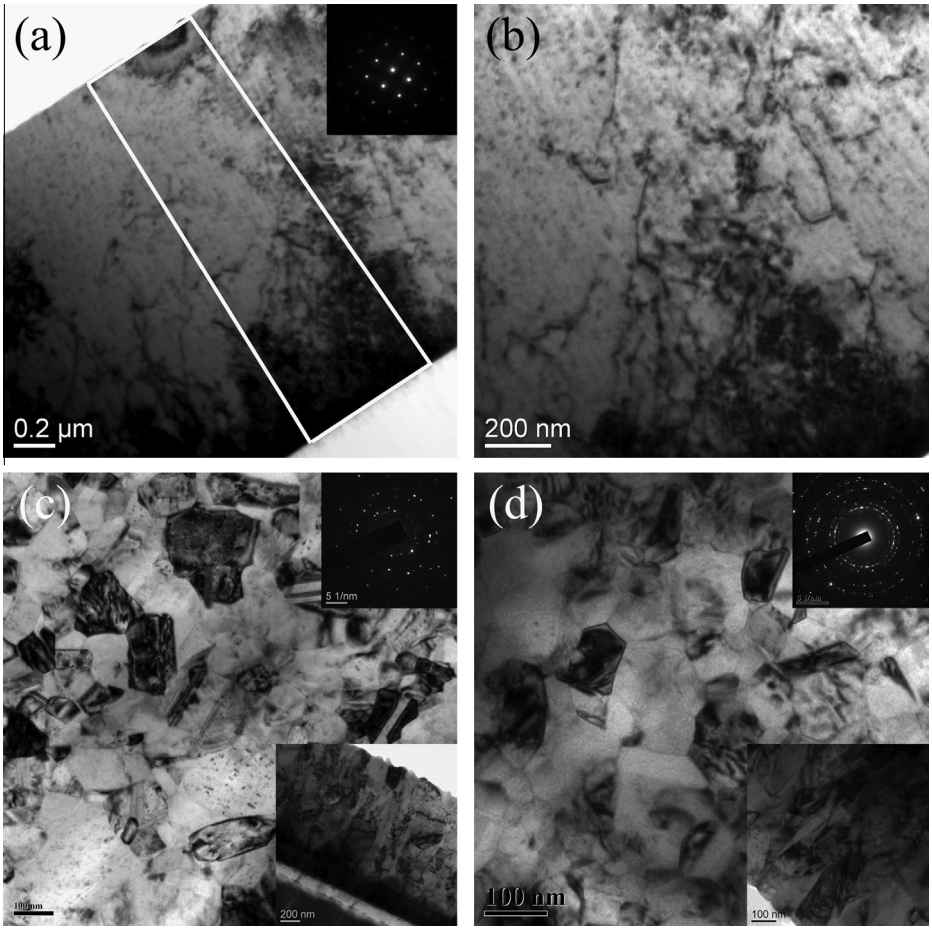

Fig. 1. (a) Bright-field cross-sectional TEM image showing the microstructure of the ⟨100⟩-SC Cu films. (b) Magnified TEM view of (a) showing the dislocation structure. The inset in (a) is the corresponding selected-area diffraction pattern (SADP). Bright-field planar TEM micrograph showing the microstructure of the MC Cu thin films with (c) a grain size of $d \approx 180$ nm and (d) a grain size of $d \approx 110$ nm. The insets in (c) and (d) are the corresponding SADPs and cross-sectional TEM images.

and b. It should be noted that not all of the dislocations are visible in a cross-sectional TEM image. In pillars with high dislocation densities, plastic deformation can occur at low mechanical stress due to the collective motion of the dislocations within the structure, and the plastic flow is relatively smoother [51–53]. This behavior is markedly different from that of pillars with low dislocation densities, which are characterized by large load drops. These load drops may be initiated by expansion of FIB-created loops at the surface of the pillars [51–53]. In contrast, the cross-sectional and planar TEM investigations showed that the PC Cu films have submicron-sized ($\sim 180 \pm 40$ nm, see Fig. 1c) and nanosized ($\sim 110 \pm 30$ nm, see Fig. 1d) grains and few planar defects (twins). Although twins can significantly enhance the strength and the SRS [54], their effect can be neglected in the present case because the number of twins is extremely low (statistically, only one or two twinned grain(s) exist(s) in a MC Cu pillar with $\phi = 1000$ nm). Some dislocations were observed in the grain interiors. The selected-area diffraction patterns (SADPs) in Fig. 1 are consistent with the XRD results. More information on the microstructure can be found elsewhere [28].

3.2. Deformation morphologies of the SC/MC Cu pillars

Fig. 2a–d shows typical SEM images taken before and after the uniaxial compression of the ⟨100⟩-SC pillars with $\phi = 650$ nm (Fig. 2a and b), $\phi = 800$ nm (Fig. 2c and d) and $\phi = 1200$ nm (Fig. 2e and f) at a strain rate of 2×10^{-4} s^{-1}. Despite the symmetric slip orientation, those samples with $\phi \leqslant \sim 650$ nm are generally prone to deformation in quasi-single-slip mode (i.e. these are limited to only one set of slip planes), whereas the samples with $\phi > \sim 800$ nm only exhibit a bulk-like multiple slip deformation that is accompanied by significant barreling. The alternative slip deformation on two or more inclined sets of slip systems, which starts at the top of the pillar and progresses down the sample height with ongoing compression, is readily observed for the intermediate-sized (650–800 nm) samples and leads to a mushroom shape. Similar results were observed in ⟨100⟩-SC Cu pillars with height-to-diameter ratios >5 by Kiener and Minor [8]. The deformation morphologies that were observed for the different sample sizes suggest that the deformation behavior is limited by the source [8]. Smaller samples with multiple slip systems,

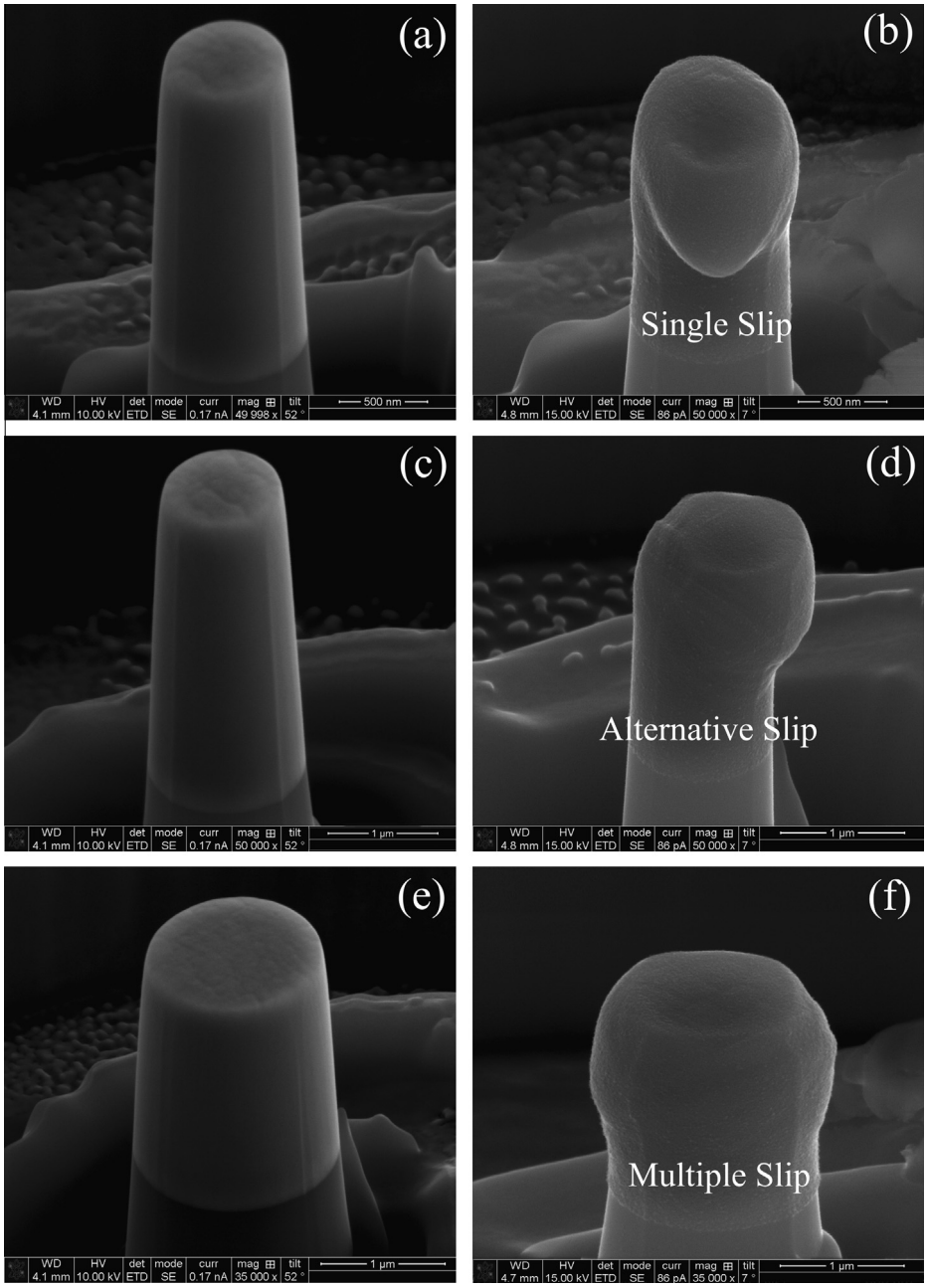

Fig. 2. Typical SEM images of the ⟨1 0 0⟩-SC Cu micropillars before and after the uniaxial compression tests. As-milled SC Cu pillars with (a) $\phi = 650$ nm, (c) $\phi = 800$ nm and (e) $\phi = 1200$ nm; (b) SC Cu pillar with $\phi = 650$ nm after compression showing single-slip deformation; (d) SC Cu pillar with $\phi = 800$ nm after compression showing alternative-slip deformation; and (f) SC Cu pillar with $\phi = 1200$ nm after compression showing multiple-slip deformation.

due to the limited number of dislocation sources in the sample volumes, deform like single-slip-oriented crystals. Larger samples exhibit an observed deformation behavior that is close to that of bulk Cu with a ⟨1 0 0⟩ orientation. Due to the tapered geometry of the pillars, the source-limited situation might become even more pronounced because tapering creates a stress gradient over the sample height, which further confines the actual deforming volume [7].

Fig. 3a–f presents representative SEM images that were taken before and after the uniaxial compression of $d = 110$ nm MC pillars with $\phi = 300$ nm (Fig. 3a and b), $\phi = 500$ nm (Fig. 3c and d) and $\phi = 800$ nm (Fig. 3e and f) at a strain rate of 2×10^{-4} s^{-1}. It is found that the smallest pillars with $\phi = 300$ nm (or aspect ratios near 7) are very likely to bend during the compression tests. At the same time, a series of multiple grain offsets is observed in the smallest Cu MC pillars (see Fig. 3b), as was also observed in $d \approx 60$ nm Ni MC pillars [42]. In contrast, all of the MC Cu pillars with $\phi \geqslant 500$ nm (or aspect ratios < 3.5) uniformly deform and exhibit significant barreling, similarly to macroscopic PC materials. The localized

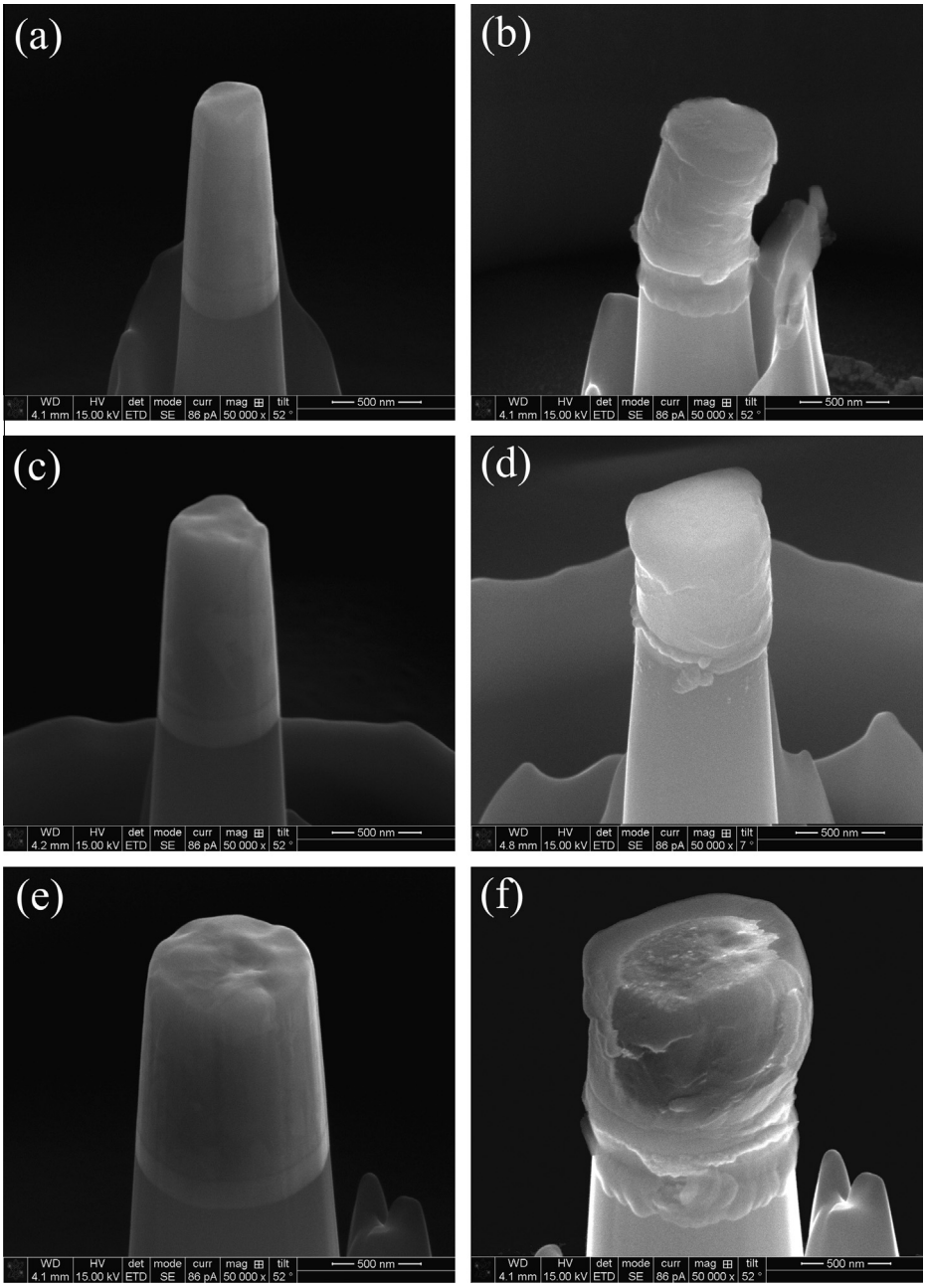

Fig. 3. Typical SEM images of the MC Cu micropillars before and after the uniaxial compression tests. As-milled MC Cu pillars with (a) $\phi = 340$ nm, (c) $\phi = 500$ nm and (e) $\phi = 800$ nm; (b) compressed MC pillar with $\phi = 340$ nm showing grain offsets, and compressed MC Cu pillars with (d) $\phi = 500$ nm and (f) $\phi = 800$ nm showing the barreling of the micropillar.

grain offset is only observed at great strains/stresses. Additionally, MC Cu FIB-fabricated pillars are rougher than SC Cu pillars, even though the same current (15 pA) was used during the fabrication processes. This result is most likely caused by the weaker resistance of GBs to Ga^+ [55]. Specifically, the deformation morphologies of all of the MC Cu micropillars are strain rate independent within this limited data set. It should be noted that the pillars are very tall with aspect ratios near 7 and often bend during the compression tests, which in turn renders the compressive stresses reported actually smaller than they should be during ideal uniaxial compression tests. Therefore, we only focus on the MC Cu pillars of great size $\phi \geqslant 500$ nm to elucidate the size effects on their plastic characteristics (discussed below).

3.3. True stress–strain curves of the SC/MC Cu pillars

Figs. 4 and 5 show representative true stress–strain curves of the $\langle 100 \rangle$-SC and MC Cu pillars for different strain rates (Figs. 4a and 5a) and different diameters (Figs. 4b and 5b). All of the true stress–strain curves are characterized by a nearly elastic loading followed by multiple stress drops and intermittent strain bursts with size ε_b,

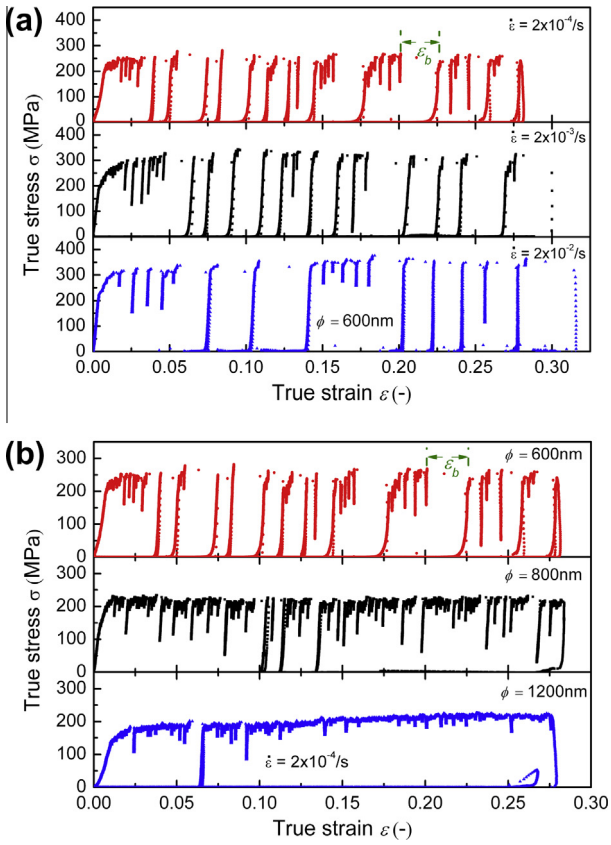

Fig. 4. True stress–strain plots for the (a) ⟨100⟩-SC Cu pillars with $\phi = 500$ nm at different strain rates and (b) for four different ⟨100⟩-SC Cu pillars with $\phi = 300$, 500, 800 and 1200 nm that were compressed at a strain rate of 2×10^{-4} s^{-1}.

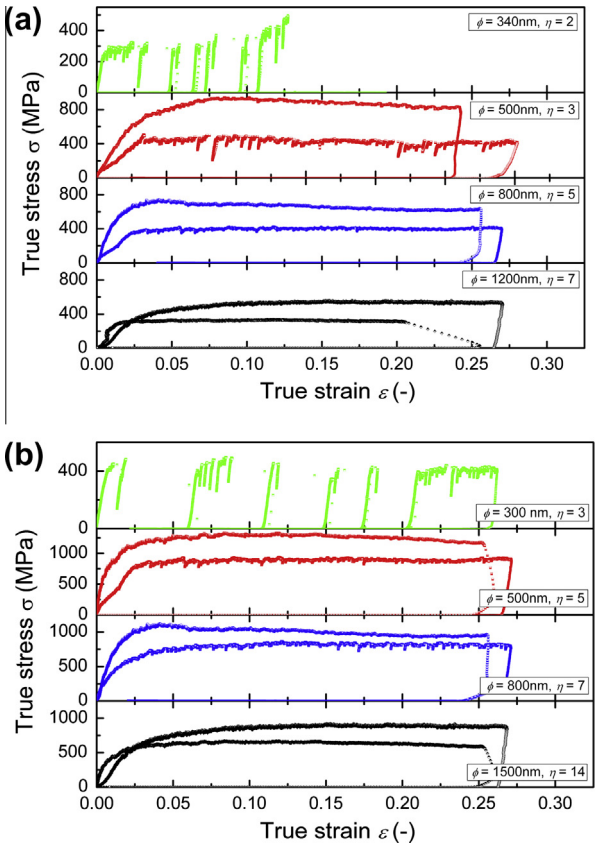

Fig. 5. True stress–strain plots for (a) MC Cu pillars with a grain size of $d \approx 180$ nm with $\phi = 340$, 500, 800 and 1200 nm and (b) MC Cu pillars with a grain size of $d \approx 110$ nm with $\phi = 300$, 500, 800 and 1500 nm that were compressed at strain rates of 2×10^{-4} and 2×10^{-2} s^{-1}. The MC Cu pillars with $\phi = 340$ and 300 nm were only compressed at 2×10^{-4} s^{-1}.

as schematically shown in Figs. 4 and 5. The stress drops are usually caused by dislocation slips (avalanches) that result from rapid dislocation emission or the sudden release of dislocations from pinned sources [12,26]. The strain bursts are ascribed to dislocation propagation [25,56] or GB-mediated processes [57,58]. In these true stress–strain curves, it is noticeable that a strain-hardening phenomenon was observed in all of the tested pillars when $\varepsilon_p < 8\%$, and this was particularly noticeable in the MC pillars at larger $\dot{\varepsilon}$. Clear dependences of σ on $\dot{\varepsilon}$ and ϕ were observed, i.e. higher $\dot{\varepsilon}$ and smaller ϕ lead to higher σ. It appears that the MC Cu pillars exhibit a transition from continuous plastic flow ($\eta > 7$) to limited ($7 > \eta > 3$) and non-existent ($\eta < 3$) flow, as shown in Fig. 5. A similar transition occurs in the ⟨100⟩-SC Cu pillars studied in the present study and in the ⟨100⟩-SC pillars analyzed in a previous study [8] in response to a reduction in ϕ. Furthermore, faster $\dot{\varepsilon}$ and larger ϕ lead to smoother stress–strain curves in the MC Cu pillars.

3.4. Effects of strain rate and sample size on the strength of SC/MC Cu pillars

Shifts in dislocation substructures generally result in corresponding shifts in deformation mechanisms of fcc metals [59]. In other words, once dislocation substructures evolve with the plastic strain ε_p (or $\dot{\varepsilon}$), the deformation mechanisms will also evolve with ε_p (or $\dot{\varepsilon}$). For example, in SC pillars, such as Cu [21,60], Au [13] and Ni [16], a transition from ordinary forest hardening to exhaustion hardening or starvation hardening can alter the power-law exponent α. (Hardening behavior is also observed in MC metals.) Thus, the choice of the characteristic flow stress should be carefully considered. Because large stress–strain scatter is generally observed in the initial stage of plastic flow during a microcompression test (which is most likely caused by the rough tip of the pillar/indenter), the strength $\sigma_{2.5}$ at a relatively large amount of plastic strain ($\varepsilon_p = 2.5\%$), which is similar to that used in previous studies [13,44,61], was chosen in the present work.

The plastic properties of small-volume MC materials are determined by their internal structure size and by the external sample size. The dependence of the strength $\sigma_{2.5}$ on $\dot{\varepsilon}$ is shown in Fig. 6a and b for the SC and MC Cu pillars, respectively, with different diameters. It can clearly be seen in Fig. 6a and b that $\sigma_{2.5}$ for both the SC and the MC Cu pillars monotonically increases with increasing $\dot{\varepsilon}$. This result is consistent with other results for ⟨111⟩-SC Cu pillars [10] and PC Cu pillars [33,54]. Compared with the SC pillars, the MC pillars exhibit a much broader variation in

the dependence of strength on $\dot{\varepsilon}$. A smaller ϕ results in a greater slope for an MC pillar with a constant d. In particular, MC pillars with different grain sizes exhibit different slopes, which vary with ϕ. It appears that, at diameters greater than $\phi \approx 1000$ nm, a larger d results in a greater slope for a given ϕ, whereas, at diameters less than $\phi \approx 1000$ nm, a larger d leads to a smaller slope. In addition, the MC Cu pillars exhibit higher strength compared with $\langle 100 \rangle$-Cu and $\langle 111 \rangle$-Cu pillars with an equivalent ϕ.

The ϕ-dependent strength $\sigma_{2.5}$ is shown in Fig. 7a and b for the SC and MC Cu pillars, respectively, at different $\dot{\varepsilon}$. The $\sigma_{2.5}$ of the SC and MC Cu pillars monotonically increases with decreasing ϕ (>300 nm), which is in agreement with the tenet "smaller is stronger" [1,2,5,6]. For comparison, the strength of $\langle 100 \rangle$-SC Cu pillars, which was measured by Kiener and Minor [8], is also plotted in Fig. 7a. It is noticeable that for larger ϕ (>300 nm) $\sigma_{2.5}$ slowly increases with decreasing ϕ ($\alpha = 0.5$), whereas for smaller ϕ (<300 nm) $\sigma_{2.5}$ markedly increases with decreasing ϕ ($\alpha = 1$). The exponent α of the present SC pillars is insensitive to $\dot{\varepsilon}$ and almost constant at ~0.5. Similarly, the dependence of α on $\dot{\varepsilon}$ is quite weak for the studied MC Cu pillars with different grain sizes, i.e. ~0.45 for larger-d MC pillars and ~0.4 for smaller-d MC pillars in the $\dot{\varepsilon}$ range studied. To provide deeper insight into the evolution of the dislocation substructure with ε_p, i.e. the possible transition in the hardening mechanisms, the strength σ_5 (at $\varepsilon_p \approx 5\%$) was also plotted against $\dot{\varepsilon}$ and ϕ for the SC and MC Cu pillars (data not shown). This strength exhibits trends similar to those obtained for $\sigma_{2.5}$.

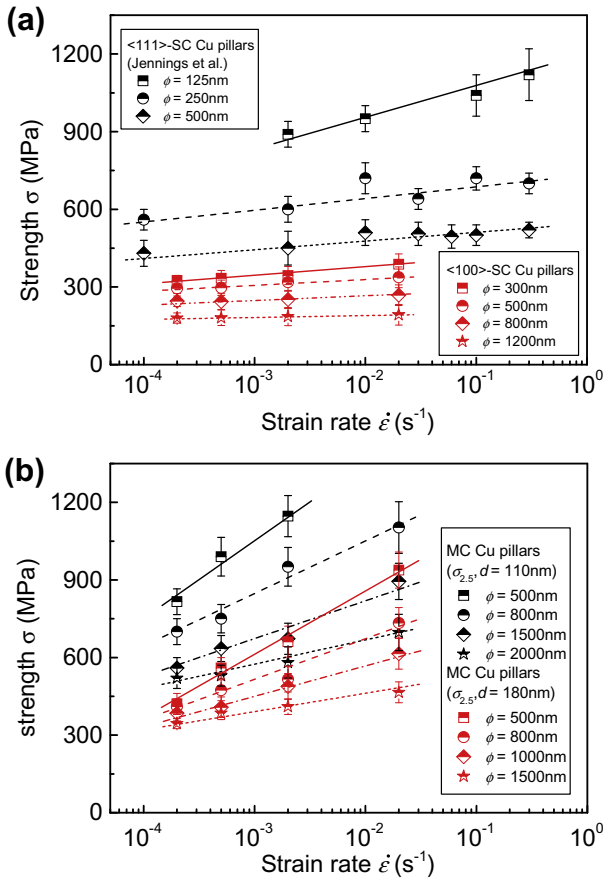

Fig. 6. (a) The strength $\sigma_{2.5}$ of the $\langle 100 \rangle$-SC pillars as a function of $\dot{\varepsilon}$. The strength σ_{10} of the $\langle 111 \rangle$-SC Cu pillars [10] with three different diameters is also plotted for comparison. (b) The strength $\sigma_{2.5}$ of the MC Cu pillars with different grain sizes as a function of $\dot{\varepsilon}$.

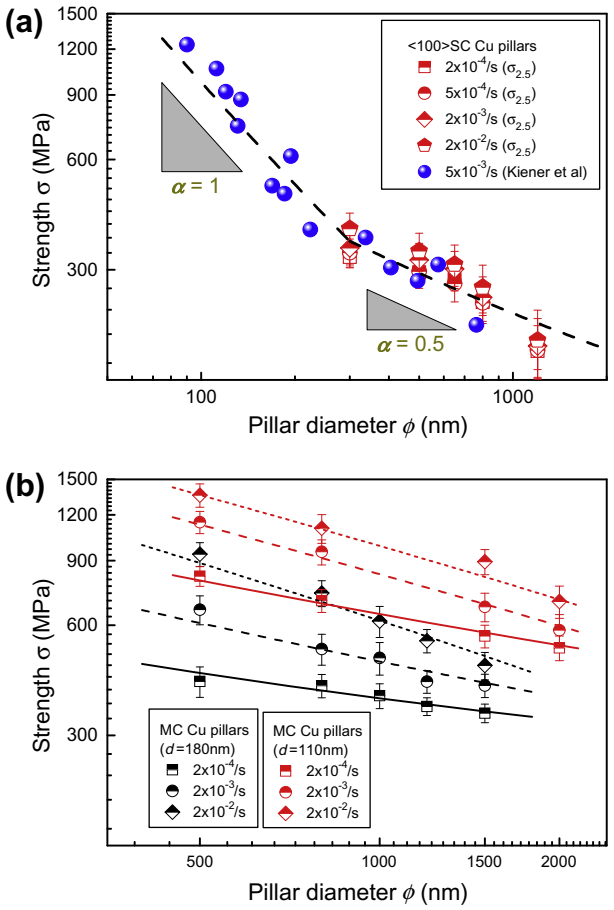

Fig. 7. (a) The strength $\sigma_{2.5}$ of the $\langle 100 \rangle$-SC pillars as a function of ϕ for different strain rates. The strength of $\langle 100 \rangle$-SC Cu pillars [8] that were compressed at $\dot{\varepsilon} = 5 \times 10^{-3}$ s^{-1} is also plotted for comparison. (b) The strength $\sigma_{2.5}$ of the MC Cu pillars with different grain sizes as a function of ϕ for different strain rates.

Fig. 8 shows the η-dependent strength $\sigma_{2.5}$ of the SC and MC Cu pillars examined in the present study and the reported strength of bulk NC Cu [33], MC Ni pillars [42], $\langle 100 \rangle$-SC Cu pillars [8] and $\langle 111 \rangle$-SC Cu pillars [10] to achieve a comprehensive understanding of the (coupling) effects of the internal and external sizes on plastic flow. The SC Cu pillars ($\eta = 1$) generally exhibit monotonically increasing strength as ϕ is reduced from the micron scale to the nanoscale. Interestingly, over this η range, the $\sigma_{2.5}$ of the MC Cu pillars first increases to a peak at a critical η (η_C) or ϕ. Below η_C, $\sigma_{2.5}$ decreases with decreasing η (or ϕ), thereby exhibiting an inverse η (or ϕ) effect, whereas, above η_C, a smaller η leads to a larger $\sigma_{2.5}$. In other words, a maximum strength is observed in the η range studied, similar to the results found for bulk NC Cu [62] and nanotwinned Cu [63]. Note that only a

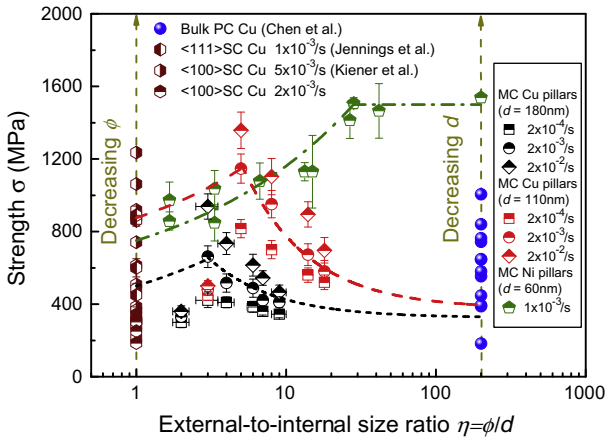

Fig. 8. (a) The strength $\sigma_{2.5}$ of small-scale ⟨100⟩-SC Cu ($\eta = 1$; measured in the present study), ⟨100⟩-SC Cu [8], ⟨111⟩-SC Cu [10], bulk-scale PC Cu [33] ($\eta = \infty$), MC Cu (measured in the present study) and MC Ni [42] pillars as a function of η, showing the strongest ϕ that emerges at the transition from bulk-scale PC metals to small-scale SC metals. All of the lines, except those corresponding to the MC Cu pillars in the softening regime ($\phi < 500$ nm), were calculated from Eq. (6).

saturation strength (corresponding to $\alpha = 0$) instead of a maximum strength has been observed in MC Ni pillars above η_C (softening is observed below this value) [42].

3.5. The SRS of the SC/MC Cu pillars

It is well known that the SRS of a material can be characterized by two key kinetic characteristics of the deformation mechanism, i.e. the SRS (m) and the activation volume (V^*) [28], both of which reflect the rate-controlling deformation process. In a thermally activated process that triggers considerable plastic flow, V^* is defined by the change in the strain rate $\dot{\varepsilon}$ with respect to the flow stress σ, the absolute temperature T, and the Boltzmann constant k_B [29]:

$$V^* = \frac{\sqrt{3}k_BT}{\sigma}\frac{\partial \ln(\dot{\varepsilon})}{\partial \ln(\sigma)} = \frac{\sqrt{3}k_BT}{\sigma m}. \quad (3)$$

This equation is consistent with the fact that the strain-rate dependence of a material is usually quantified by the power-law relation $\sigma = \sigma_0\dot{\varepsilon}^m$. The $\dot{\varepsilon}$ dependence, which is indicative of the rate-controlled mechanism, for the dislocation source operation can also be described by an Arrhenius form that correlates $\dot{\varepsilon}$ with σ [10]:

$$\dot{\varepsilon} = \dot{\varepsilon}_0 \exp\left(-\frac{\Delta G^*}{k_BT}\right) = \dot{\varepsilon}_0 \exp\left(-\frac{Q^* - \sigma V^*(\sigma, T)}{k_BT}\right), \quad (4)$$

where $\dot{\varepsilon}_0$ is a constant, ΔG^* is the activation Gibbs free energy for the stress-assisted, thermally activated process, which is controlled by the local stress/energy, and Q^* is the Helmholtz free energy (activation energy) for overcoming obstacles to dislocation motion. ΔG^* is a decreasing function of the effective stress σ because the activation barrier is lowered by the work that is done by the effective stress $\sigma V^*(\sigma, T)$.

We determined the SRS m and the activation volumes V^* for all of the compressed Cu pillars (except for the MC pillars with $\phi < 500$ nm) at different strain rates that spanned more than two orders of magnitude. The determined values of m were in the ranges of 0.01–0.04 and 0.05–0.178 for the ⟨100⟩-SC and the MC Cu pillars, respectively. The SRS m of MC Cu decreases with increasing ϕ and is much greater than that of SC Cu with a similar external size, as shown in Fig. 9a. This result indicates that the introduction of GBs can markedly enhance the SRS in small-volume SC materials. It also appears that the strain effect on the SRS of the SC pillar is quite weak, whereas its effect on the SRS of the MC Cu pillars is marked. The m for the MC pillars increases with decreasing ε_p for a fixed ϕ, similarly to that observed with nanotwinned Cu [64]. To better elucidate the internal feature size and external sample size effects on the SRS, we plotted the curve of m as a function of η for the MC pillars and compared it with that of bulk PC ($\eta = \infty$) Cu at different grain sizes [33] and for

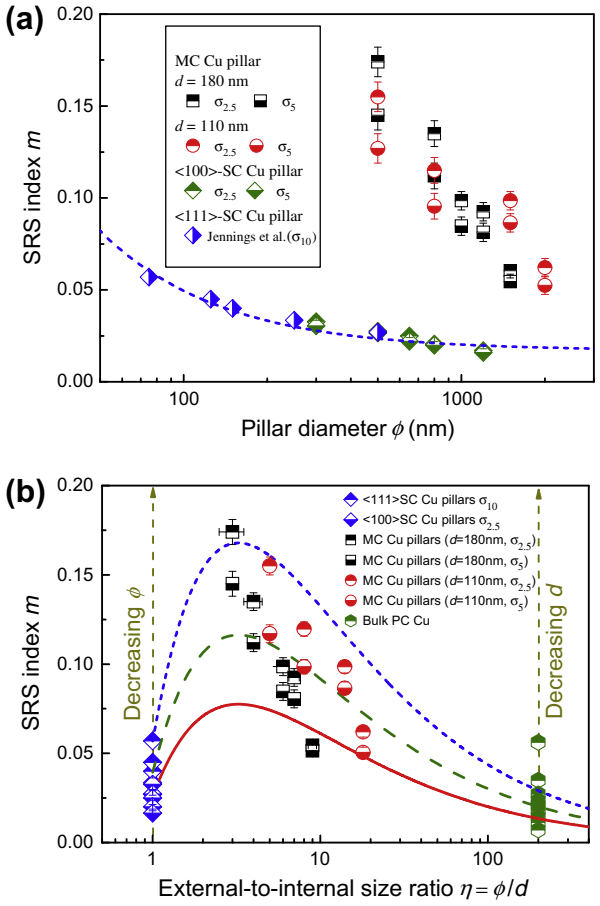

Fig. 9. (a) The SRS index m of the MC Cu pillars and small-scale ⟨100⟩-SC Cu pillars (measured in the present study) for strains of ~2.5% and ~5% and that of ⟨111⟩-SC Cu pillars [10] for a strain of ~10% as a function of ϕ. (b) A comparison of the SRS index m for the MC Cu pillars, small-scale ⟨100⟩-SC Cu pillars at two different strains (2.5% and 5%), ⟨111⟩-SC Cu [10] pillars ($\eta = 1$), and bulk-scale PC Cu [33] ($\eta = \infty$), showing the maximum m that emerges at a critical η or ϕ at the transition from bulk-scale PC metals to small-scale SC metals. The lines were obtained from the combination of Eqs. (3) and (10).

SC Cu at different diameters [10], as shown in Fig. 9b. Interestingly, a maximum in the SRS m was also observed for the MC Cu pillars at a critical η (η_C). Below η_C, the SRS m decreases with decreasing η, and, above η_C, a smaller η leads to a higher SRS m.

The activation volume V^* is generally inversely proportional to the SRS m. It is possible to gain insight into the microstructural plasticity mechanisms that are responsible for this surprisingly high SRS in the MC Cu pillars by analyzing their activation volumes. The ϕ -dependent V^* of the MC pillars is shown in Fig. 10a. The V^* of the MC pillars decreases with decreasing ϕ and scales approximately linearly with ϕ. Similarly, the $\langle 100\rangle$-SC Cu pillars exhibit a monotonically decreasing V^* with decreasing ϕ, which is in agreement with the behavior obtained with $\langle 111\rangle$-SC Cu pillars [10]. Additionally, the V^* of the MC Cu pillars with $\phi \geqslant 500$ nm decreases with decreasing d, analogously to bulk PC Cu [33] (see the inset in Fig. 10b). Notably, the V^* determined in this study is $\sim 20b^3$ for the MC pillars with $\phi = 1500$ nm and decreases to $\sim 4b^3$ for the MC pillars with $\phi = 500$ nm. In contrast, the V^* of SC pillars almost linearly decreases from $\sim 150b^3$ to $\sim 10b^3$ when ϕ is reduced from 1200 to 75 nm [10]. It appears that SC, MC and PC Cu exhibit the following characteristic: the activation volume V^* scales with their characteristic size D.

4. Discussion

4.1. Influence of sample fabrication on mechanical properties

To date, FIB milling is the most commonly used method to fabricate micro- and nanopillars to study small-scale plasticity and size effects in uniaxial compression [5,6]. However, FIB milling can introduce defects into the milled pillars by forming dislocation loops and surface amorphization [65,66]. Damage of this type is a known source of strengthening in bulk single crystals, implying that FIB-fabricated pillars may be stronger than bulk [67–69]. Therefore, as the relative surface area to volume ratio in pillars increases with decreasing pillar size, these ion damage effects become more adverse. Several recent findings have shown that FIB-free, pristine pillars yield at near-theoretical strength [52,70,71]. However, it has been shown that initially defect-free NiAl–Mo eutectic alloys undergo a significant decrease in strength after exposure to the FIB or pre-strain as a result of increasing damage/dislocation density [67,68]. Specifically, Jennings et al. [11] have pointed out that it is the initial dislocation density rather than the fabrication technique that drives the size effect in fcc metals. This finding is consistent with previous work on body-centered cubic alloy systems [67,68,72], showing that the pillar strength is a strong function of the initial dislocation density.

In our experiments, the low beam current (15 pA) used in the fabrication process probably minimizes the damage of the samples. However, the electron/ion beam still causes surface damage (e.g. roughness) of the samples. The

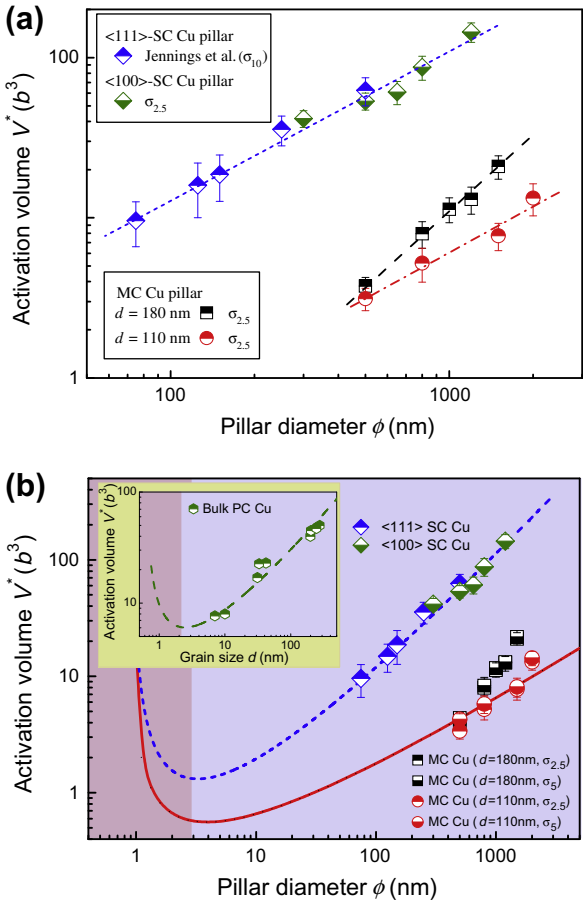

Fig. 10. (a) The activation volume of the MC Cu pillars and small-scale $\langle 100\rangle$-SC Cu pillars (measured in the present study) for a strain of ~2.5% and that of $\langle 111\rangle$-SC Cu pillars [10] for a strain of ~10% as a function of ϕ. (b) A comparison of the activation volume (V^*) of the MC Cu pillars, small-scale $\langle 100\rangle$-SC Cu pillars and $\langle 111\rangle$-SC Cu pillars [10]. The activation volume (V^*) of bulk-scale PC Cu [33] was also plotted in the inset of (b). The lines were calculated based on the phenomenological model shown in Eq. (10).

roughness of the sample can lead to a broad variation in the initial stiffness of the material but does not significantly affect the strength [8]. Indeed, we have noticed that the slope of loading curve is smaller than that of unloading curve. To circumvent the FIB milling effects on the strengths of all of the samples, strengths $\sigma_{2.5}$ and σ_5 were chosen for the following discussion.

4.2. Deformation crossover-induced strongest external size of the MC Cu pillars

The classical methods for the strengthening of materials rely on strategies that judiciously control the generation of and interactions among internal defects, such as boundaries and dislocations [31,73–75]. In bulk ultrafine-crystalline ($d \approx 100$–1000 nm) materials, GBs obscure the passage of gliding dislocations and hence elevate the crystalline strength, and plastic deformation is sustained by dislocations that are emitted from the GBs [29,76,77]. Due to the strong constraining effect from surrounding grains,

GB-mediated mechanisms, such as GB sliding and grain rotation, are difficult to produce in samples with submicron-sized grains [29,31]. As observed in Fig. 6, the $\sigma_{2.5}$ of the MC pillars ($\phi \geqslant 500$ nm) is much higher than that of the $\langle 100 \rangle$-SC pillars for a similar/identical ϕ and a given $\dot{\varepsilon}$. The underlying reasons for this behavior are that (i) the compatibility condition at the GBs exerts an additional constraint on the deformation, and (ii) the GBs hinder the motion of the dislocations [41,58]. Additionally, the SRS m of the MC Cu pillars ($m \approx 0.1$–0.18) is markedly less than that caused by GB-mediated deformation ($m \approx 0.5$), which indicates that a dislocation-mediated mechanism dominates the deformation [31]. For the MC pillars, the marked increase in strength with decreasing sample size can be attributed to the reduced length of the dislocation source, which needs a higher stress to be activated [39]. Similar observations have been reported in nanocrystalline ($d \approx 30$ nm) Ni [39] and ($d \approx 35$ nm) Zr pillars [78]. However, if $\phi < 500$ nm, the strength of the MC Cu pillars sharply decreases to even less than that of the corresponding SC Cu pillars because the grain number across the diameter of the MC pillars is ~2–3, which leads to free-side-surface failure and grain offsets caused by grain movement (Fig. 3b). This phenomenon is consistent with the observations reported by Jang et al. for electroplated MC Cu pillars with $d \approx 160$ nm and $\phi = 500$ nm [58]. Therefore, it is conceivable that the role of the GBs shifts to that of the deformation path itself such the GB-mediated mechanism instead of the dislocation-driven process is responsible for the strength reduction in these MC pillars. Thus, two competing processes emerge simultaneously upon the introduction of internal interfaces into MC pillars with a smaller d: Hall–Petch-like strengthening and GB-mediated weakening. If the dislocation-driven process overwhelms the GB-mediated mechanism, the samples exhibit monotonically increased strength [39]; otherwise, the samples show monotonically decreased strength [41]. The crossover of these two mechanisms determines the strongest ϕ in the MC Cu pillars and leads to the peak strength [78]. Additionally, these two competing effects can cause saturation strength if these two mechanisms balance at an external length-scale rather than a critical sample size, as in the case of MC Ni pillars with $d \approx 60$ nm and ϕ ranging from 100 to 2500 nm [42]. Therefore, the fundamental difference between the MC Cu pillars analyzed in the present study (peak strength) and MC Ni pillars (saturation strength) can be attributed to the (combined) effect(s) of microstructure and orientation [58] because the GB-mediated and dislocation-driven processes can switch on simultaneously [57].

Additionally, it can be seen in Fig. 8 that the critical ratio η_C for softening MC pillars increases from ~3 to ~5 to ~30 when d decreases from ~180 to ~110 to ~60 nm. The critical d (e.g. 60 nm [42]) that is observed for softening in the MC pillars is much larger than the value of ~15–20 nm for bulk NC metals. This result suggests that a reduction in the external sample size activates GB-mediated processes, in contrast to the dislocation-driven mechanisms that govern plasticity in submicron-sized and nanosized ($d > 50$ nm) bulk PC metals. It appears that a smaller d results in a higher possibility of GB-mediated mechanism in smaller MC pillars [41,57]. Specifically, in the smallest ($\phi \approx 340$ nm) MC pillars, the operation of (localized) GB-mediated processes likely causes misalignment in the compression test, which results in a slight bending of the pillars (see Fig. 3b) [57] and in underestimating the actual strength of the sample. The following discussions on the size-driven strength and SRS of the MC Cu pillars are mainly focused on the strengthening regime, i.e. $\phi \geqslant 500$ nm.

4.3. Scaling behavior of the strength in the SC/MC Cu pillars

In small-scale materials, the stress that is required to produce a dislocation from a source with length S is proportional to $(1/S)\ln(S/b)$ [2,6]. The distribution of the nucleation stress is compared to a power law, which is used to describe the size effect in tension or compression tests [2,6]:

$$\sigma = \sigma_0 + C_1\sqrt{\rho} + \frac{C_2}{S}\ln\left(\frac{S}{b}\right) \approx AD^{-\alpha}, \tag{5}$$

where the first term in the middle corresponds to friction stress, the second term is due to back-stresses from dislocation–dislocation interactions, and the last term originates from the source strength. C_1 and C_2 are proportionality factors, D is the characteristic size (e.g. ϕ and d), and α is the strength scaling exponent. A size effect will be found in the experiments if the initial source length scales with the external sample size or the internal structure size. This phenomenon was verified with the SC Cu pillars with $\alpha = 0.5$ analyzed in the present study for all strain rates, as shown in Fig. 7a. Interestingly, as observed in Fig. 7a, when the SC pillar size ϕ is greater than ~300 nm, $\alpha = 0.5$, and, below this size, $\alpha = 1$. This result potentially indicates a change in the governing deformation mechanism because, below this transition length, the scaling follows a D^{-1} behavior, which is indicative of dislocation nucleation-controlled plasticity [1,2,5,6,21]. Above this size, the strength scales close to $D^{-0.5}$, which is typically associated with dislocation interaction processes [1,2,5,6,21].

Although the analyzed MC sample exhibits a characteristic length scale smaller than the pillar diameter, an external sample size effect was observed. The strength $\sigma_{2.5}$ increases with decreasing ϕ (σ_5 behaves the same way), which can be described by Eq. (5) with $\alpha = 0.45$ and 0.4 for the MC Cu pillars with $d = 180$ and 110 nm, respectively, at different strain rates. The reduction in α with decreasing d implies that an increase in η or ϕ can more markedly reduce the sample size effect on the plastic flow for smaller-d-sized MC pillars. This result is (partly) supported by the experimental findings that the peak strength was observed for the MC Cu pillars with $d = 180$ and

110 nm, whereas the saturation strength was observed for the MC pillars with $d = 60$ nm (see Fig. 8). In particular, the MC pillars have a lower α for the strength dependence on ϕ than the SC Cu pillars because the flow stress of the MC pillars is mainly controlled by their internal features. It should be noted that the power exponent α increases with increasing ε_p from 2.5% to 5%, and this finding is consistent with other reported works [13,16]. This result indicates that a transition in the hardening behavior, i.e. from starvation hardening to ordinary forest hardening, occurs in the MC Cu pillars [28]. More details on this transition can be found elsewhere [28].

The lack of an $\dot{\varepsilon}$ effect on α for both the larger-sized SC and MC pillars ($\phi > \sim 500$ nm) demonstrates that the mechanism that is responsible for the power law is insensitive to $\dot{\varepsilon}$ because the $\dot{\varepsilon}$ dependence would manifest itself as a deviation from the power law [10]. However, we note that Eq. (5) only takes into account athermal effects; thus, the ability of this equation to describe the thermally activated processes that are discussed here is inadequate, particularly for the MC Cu pillars. A more accurate expression for Eq. (5) could be obtained by including the $\dot{\varepsilon}$ effects or the thermal activation contribution [10]:

$$\sigma^* = \sigma - \frac{k_B T}{V^*} \ln\left(\frac{k_B T N \upsilon_0}{E_{Cu} \dot{\varepsilon} V^*}\right), \tag{6}$$

where υ_0 is the attempt frequency, N is the number of equivalent dislocation nucleation sites, E_{Cu} denotes the apparent Young's modulus of Cu, and the other symbols have the same meanings as before. In a previous section, we demonstrated that the measured V^* varies nearly linearly with D. This result implies that the thermal contribution (which scales with $\frac{1}{V^*}\ln\left(\frac{1}{\dot{\varepsilon}V^*}\right)$) is proportional to $\frac{1}{D}\ln\left(\frac{1}{\dot{\varepsilon}D}\right)$. If the source length S in Eq. (6) and the characteristic size D are linearly correlated, both the thermal and the athermal components of a dislocation source will have almost the same size-dependent behavior because their size dependencies will be dominated by the pre-logarithm $1/D$ dependence. This added thermal contribution to Eq. (6) should include the correct trend in the $\dot{\varepsilon}$ dependence: a decrease in $\dot{\varepsilon}$ rigidly shifts the power law to lower stresses for both the SC and the MC samples. The variation in strength as a function of η for the analyzed MC Cu pillars with different grain sizes in the hardening regime ($\phi \geqslant \sim 500$ nm) can be well captured by Eq. (6) using $\alpha = 0.45$ for the MC pillars with $d = 180$ nm at different strain rates, $\alpha = 0.4$ for the MC pillars with $d = 110$ nm at different strain rates, and $\alpha = 0$ for MC Ni pillars with $d = 60$ nm, as shown in Fig. 8. The reduction in α with decreasing d (partially) supports the transition of the peak strength in larger-d-sized MC pillars to the saturation strength in smaller-d-sized MC pillars and indicates that the GB-mediated mechanism is initially preferred in smaller-d-sized MC materials. However, in the softening regime ($\phi < \sim 500$ nm), the dependence of strength on ϕ follows $\sigma \propto \phi^{0.375}$ for MC Ni samples (the curves for the MC Cu pillars are only visual guides due to limited data being available).

4.4. Size- and strain-dependent SRS of the SC/MC Cu pillars

In both small-scaled SC and bulk PC metals, such as Cu, the SRS m monotonically increases with decreasing characteristic size D. Surprisingly, the presented results have unambiguously revealed that the introduction of internal GBs and/or the shrinkage of the sample size can remarkably increase the SRS of metals and that a maximum SRS m in the MC Cu pillars emerges upon the reduction of η to a critical η_C. The free surface-to-volume ratio sharply increased with decreasing η or ϕ. This result can enhance the surface image force effect, which can drag dislocations out of the pillars, on the SRS of the pillars [79,80]. Therefore, a smaller η leads to a higher m. Conversely, the internal GB-to-volume ratio dramatically decreased with decreasing η or ϕ, which results in a weakening of the role that the GBs play in the SRS and a reduction in the SRS m. The competition between the free surface and the internal GBs thus contributes to the maximum SRS m of the MC pillars. Additionally, the higher m found in this study compared with the reported m for NC Cu [33], and even for $\langle 1\,1\,1\rangle$-SC Cu pillars [10] with similar sizes, indicates additional dislocation–boundary interactions in the MC pillars [81].

For the SC pillars analyzed in the present study, the SRS m that was obtained at different strains (or stress levels, e.g. $\sigma_{2.5}$ and σ_5) has almost the same values within the scatter, which implies that the dislocation substructures do not significantly evolve with the plastic strain ε_p. The multiplication and interaction of the internal dislocations that generated from bulk sources should control the plastic flow with increasing ε_p [80] because pre-existing dislocations are difficult to mechanically anneal [19,28]. This phenomenon is supported by the large V^* of $\sim 40b^3$–$150b^3$ [10]. Forest/exhaustion hardening most likely contributes to the enhanced strength at high ε_p. In contrast, the extremely small V^* of $\sim 4b^3$–$20b^3$ for the MC pillars analyzed in the present study indicates that the GB/surface emission of the dislocations sustains plastic deformation [10]. The absence of hardening at low $\dot{\varepsilon}$ indicates that the dislocations created from the GBs/surface can run across the grain interior and be completely absorbed by and/or annihilated at the GBs/surface [28,82]. One of the consequences of an equal dislocation nucleation and absorption rate is that the internal microstructure should not appreciably change as a function of ε_p, which enables the use of a flow stress at $\varepsilon_p = 2.5\%$ or even at $\varepsilon_p = 5\%$ in the estimation of the SRS (m or V^*) for the MC Cu pillars. However, at high $\dot{\varepsilon}$, the hardening phenomenon that is observed in the MC pillars implies that the dislocation substructures indeed evolve with ε_p, i.e. dislocation accumulation and interaction (ordinary forest hardening) exist in lieu of starvation. The propensity for dislocations to escape at the free surfaces of the nanocrystals enables the shift in the governing plasticity mechanism from the ordinary forest hardening to the source activation dominated processes. This

phenomenon was verified by the reduced m (and increased α) at larger ε_p.

To elucidate the size and strain effects on the SRS m, we consider the fact that the plastic flow of the MC Cu pillars should be dominated by GB Frank–Read sources (FRSs), whereas the SC Cu pillars should be deformed by internal FRSs and single-arm sources (SASs, which can either be formed by the truncation of FRSs at free surfaces or directly generated in initial dislocation structures). We derived the SRS m for SC and MC Cu pillars in our previous work [28], similarly to Cheng et al. [32], and these can be respectively expressed as:

$$m = \frac{\sqrt{3}k_B T}{b\chi}\frac{1}{C_1\xi + C_2\xi/\sqrt{\rho\phi}} \tag{7a}$$

and

$$m = \frac{\sqrt{3}k_B T}{b\chi}\frac{1}{\zeta(C_1\sqrt{\rho}d + C_2\sqrt{d})}. \tag{7b}$$

The variable χ is the distance (on the order of b) that is swept out by a mobile dislocation during one activation event and is approximately constant, ξ and ζ are proportionality factors, and ρ is the total dislocation density, which can be correlated with the plastic strain $\rho = \varepsilon_p/(b\lambda)$ [83], where λ is the mean free path of dislocation slips and is proportional to ϕ or d. We found that the SRS m that is calculated from Eq. (7b) changes markedly for MC pillars at different strains and is almost constant for SC pillars (according to Eq. (7a)).

4.5. Scaling behavior of the activation volume in the SC/MC Cu pillars

As mentioned previously, an effective microtesting method for inferring the rate-controlling deformation mechanisms is to determine V^* [10]. In the present work, the V^* of all of the MC samples covers a narrow range from $\sim 4b^3$ to $20b^3$, whereas that of the SC Cu pillars falls in the range from $40b^3$ to $150b^3$. It has been suggested that MC pillars deform via the activation of GB sources that nucleate dislocations, whereas SC pillars deform via the collective dislocation dynamics that invoke dislocation multiplication, propagation and interaction [10].

In this study, we attempted to develop a phenomenological model that quantitatively describes the relationship between V^* and D (e.g. ϕ or d) by simply assuming that the dislocation source length (S) is a strong function of D, i.e. $S \approx \kappa D$, where κ is a scaling coefficient. This model takes into account the Orowan–Frank–Read process [84] and approximates a SAS as half of a FRS such that the activation volume and energy of a SAS corresponds to that of half of a FRS. Based on Nabarro's derivation for the activation volume of a FRS [85], under a given applied shear stress, a dislocation segment that is pinned by two immobile pinning points has two equilibrium positions, which correspond to the same radius of curvature. To create a new dislocation from a FRS, a certain amount of thermal energy is needed to move the dislocation segment between the stable and the unstable equilibrium positions. The V^* that is associated with this activation event can be given by [85]:

$$V^* = \frac{1}{2}bS^2\left(\frac{\tau_c^*}{\tau^*}\right)^2\left[\arccos\left(\frac{\tau^*}{\tau_c^*}\right) + \frac{\tau^*\left[(\tau_c^*)^2 - (\tau^*)^2\right]^{1/2}}{(\tau_c^*)^2}\right]$$
$$\approx bS^2\sqrt{\frac{2(\tau_c^* - \tau^*)}{\tau_c^*}}, \tag{8}$$

where τ^* is the shear stress that is needed to bow out the dislocation segment with a radius of curvature R and τ_c^* is the athermal strength of a FRS that corresponds to $R = S/2$. These parameters can be expressed as [84] $\tau^* = \frac{\mu_{Cu}b}{2R}f(S)$ and $\tau_c^* = \frac{\mu_{Cu}b}{S}f(S)$, where $f(S) = \frac{1}{2\pi(1-\nu)}[(1-\frac{3}{2}\nu)\ln(\frac{S}{b}) + \frac{\nu-2}{2}]$ is a factor that includes the size-dependent dislocation line tension in the form of the energy per unit length of dislocation. The activation energy for a dislocation to overcome the barrier is then derived as [85] $\Delta G^* = \frac{2}{3}(\tau_c^* - \tau^*)V^*$. We thus obtain the following approximate scaling relation between the V^* and the athermal strength of Cu pillars [84,85]:

$$V^* = \left[\frac{3\beta b k_B T}{\mu_{Cu}f(S)}\right]^{1/3}(\tau_c^*)^{-5/3}$$
$$= \frac{b^{-4/3}}{\mu_{Cu}^2}\left[\frac{3\beta k_B T}{f(S)}\right]^{1/3}\left[\frac{f(S)}{S}\right]^{-5/3}, \tag{9}$$

where β is the logarithm of the atomic vibration number during an experiment [85].

As shown in Fig. 7, in the range of power-law strengthening for different strain rates, $\sigma_{2.5}$ increased with increasing $\dot{\varepsilon}$. However, the exponent α appears to be insensitive to $\dot{\varepsilon}$ for both the SC and the MC Cu pillars, which implies that the variation in the athermal strength with D reflects the commonly reported power law. Thus, we give V^* as a function of D by

$$V^* \approx \frac{b^{-4/3}}{\mu_{Cu}^2}\left[\frac{3\beta k_B T}{f(\kappa D)}\right]^{1/3}\left[\frac{f(\kappa D)}{D}\right]^{-5\alpha/3}. \tag{10}$$

Comparing the ϕ dependence of V^* to the experimental data that are presented in this study, we found that $V^* \propto \phi^{0.75}$ for the MC micropillars and $V^* \propto \phi^{1.25}$ for the SC micropillars. In the present work, the exponent α was found to be $\sim$0.4–0.45 for the MC Cu pillars and $\sim$0.5–1 for the SC Cu pillars (an exponent of $\alpha \approx 1$ was found by Kiener et al. [21]). This result leads to a range of possible exponents of $\sim$0.67–0.75 for the MC pillars (solid line) and of $\sim$0.83–1.67 for the SC Cu pillars (short-dashed line) for the relationship of V^* to ϕ. It has been postulated, however, that the exponent α cannot exceed 1 [86]. Additionally, this phenomenological model fits well the reported data for bulk NC Cu ($V^* \propto d^{0.85}$), as shown by the dashed line in the inset of Fig. 10b. The combination of our experimental

findings with those predicted by the model indicates that Frank-Read-type sources strongly contribute to the size-driven strength in the SC/MC Cu pillars, even in nanostructured PC Cu. Interestingly, we note that this model predicts a non-monotonic behavior for V^* over the whole range of D for all of the SC, MC and PC Cu materials, i.e. V^* decreases with decreasing D to a minimum at $D \approx 2.5$ nm, below which V^* sharply increases upon a further reduction in D, as shown in Fig. 10b. This probably indicates that as the characteristic size D shrinks below 2.5 nm, the FRSs/SASs become much more difficult to activate, and as a consequence the Orowan–Frank–Read process likely switches off. Specifically, dislocations can annihilate at internal GBs and surfaces of the specimen at such length-scales due to image force effects [79,87] and internal stresses [82,88], leading to the failure of this model. In these cases, other mechanisms, e.g. GB-mediated processes, and diffusive plasticity likely switch on [89,90]. Naturally, the combination of Eqs. (3) and (10) predicts a non-monotonic behavior for the SRS m of Cu materials with decreasing external sample size, as indicated by the three fitting curves shown in Fig. 9b.

5. Conclusions

By comparing the plastic deformation characteristics, i.e. the flow strength, the SRS and the activation volume, of submicron-sized SC/MC Cu pillars, we demonstrated a notable effect of both the strain rate and the (internal and external) size on the compressive flow of small-scale SC/MC Cu pillars. These findings provide insight into the possibility of tailoring both the internal feature size and the external sample dimensions to produce the desired plasticity. The main findings are summarized as follows:

(1) The appropriate introduction of GBs into the SC micropillars, which suffer from an inherent intermittent and stochastic nature, can dramatically improve the smoothness of the plastic flow in a controlled manner and significantly enhance their strength and SRS.
(2) Unlike the SC Cu micropillars, which have monotonic-size-dependent strength, a deformation crossover leads to the strongest external sample size in the MC Cu micropillars, similar to the findings observed in bulk-scale NC metals, such as Cu. Above the strongest external sample size, due to the blocking of the dislocation motion by the GBs, the "smaller is stronger" paradigm holds true, whereas, below this size, the GB-mediated mechanism causes the inverse size effect ("smaller is weaker").
(3) A maximum in the SRS emerges as the external sample size is decreased from bulk-scale nanostructured metals to small-scale SC nanopillars due to the coupling effects of the free surface and the internal GBs. This high SRS (and low activation volume) of the MC Cu micropillars arises from the operation of a GB source with a highly thermal nature instead of an internal bulk source, such as the one that pre-exists in the SC Cu micropillars. A phenomenological model was developed to quantitatively account for the scaling behavior of the activation volume with the characteristic size of the Cu pillars by considering the Orowan–Frank–Read process for FRSs and SASs.

Acknowledgements

This work was supported by the National Natural Science Foundation of China (Grant Nos. 51321003, 51322104, 51201123), the 973 Program of China (Grant No. 2010CB631003), and the 111 Project of China (B06025). G.L. is grateful for support from Fundamental Research Funds for the Central Universities and the Tengfei Scholar project. J.Y.Z. thanks the China Postdoctoral Science Foundation (2012M521765) and the Shaanxi Province Postdoctoral Scientific Research Projects for partial financial support. Access to the nanoindentation and FIB equipments in CAMP-Nano is also acknowledged.

References

[1] Greer JR, De Hosson JTM. Prog Mater Sci 2011;56:654–724.
[2] Dehm G. Prog Mater Sci 2009;54:664–88.
[3] Uchic MD, Dimiduk DM, Florando JN, Nix WD. Science 2004;305:986–9.
[4] Arzt E. Acta Mater 1998;46:5611–26.
[5] Uchic MD, Shade PA, Dimiduk DM. Annu Rev Mater Res 2009;39:361–86.
[6] Kraft O, Gruber PA, Mönig R, Weygand D. Annu Rev Mater Res 2010;40:293–317.
[7] Kiener D, Motz C, Dehm G. Mater Sci Eng A 2009;505:79–87.
[8] Kiener D, Minor AM. Acta Mater 2011;59:1328–37.
[9] Kiener D, Grosinger W, Dehm G, Pippan R. Acta Mater 2008;56:580–92.
[10] Jennings AT, Li J, Greer JR. Acta Mater 2011;59:5627–37.
[11] Jennings AT, Burek MJ, Greer JR. Phys Rev Lett 2010;104:135503.
[12] Friedman N, Jennings AT, Tsekenis G, Kim J-Y, Tao M, Uhl JT, et al. Phy Rev Lett 2012;109:095507.
[13] Maaß R, Van Petegem S, Ma D, Zimmermann J, Grolimund D, Roters F, et al. Acta Mater 2009;57:5996–6005.
[14] Maaß R, Uchic MD. Acta Mater 2012;60:1027–37.
[15] Schneider AS, Kaufmann D, Clark BG, Frick CP, Gruber PA, Monig R, et al. Phys Rev Lett 2009;103:105501.
[16] Frick CP, Clark BG, Orso S, Schneider AS, Arzt E. Mater Sci Eng A 2008;489:319–29.
[17] Zimmermann J, Van Swygenhoven H, Van Petegem S, Borca C. Acta Mater 2012;60:4614–22.
[18] Zimmermann J, Van Swygenhoven H, Marichal C, Van Petegem S, Borca C, Bartova B, et al. Acta Mater 2012;60:4604–13.
[19] Shan ZW, Mishra RK, Asif SAS, Warren OL, Minor AM. Nat Mater 2008;7:115–9.
[20] Greer JR, Nix WD. Phys Rev B 2006;73:245410–.
[21] Kiener D, Minor AM. Nano Lett 2011;11:3816–20.
[22] Oh SH, Legros M, Kiener D, Dehm G. Nat Mater 2009;8:95–100.
[23] Mompiou F, Legros M, Sedlmayr A, Gianola DS, Caillard D, Kraf O. Acta Mater 2012;60:977–83.
[24] Rao SI, Dimiduk DM, Parthasarathy TA, Uchic MD, Tang M, Woodward C. Acta Mater 2008;56:3245–59.

[25] Tang H, Schwarz KW, Espinosa HD. Phys Rev Lett 2008;100:185503.
[26] Dimiduk DM, Woodward C, Lesar R, Uchic MD. Science 2006;312:1188–90.
[27] Csikor FF, Motz C, Weygand D, Zaiser M, Zapperi S. Science 2007;318:251–4.
[28] Zhang JY, Liu G, Sun J. Int J Plasticity 2013;50:1–17.
[29] Dao M, Lu L, Asaro RJ, De Hosson JTM, Ma E. Acta Mater 2007;55:4041–65.
[30] Schiotz J, DiTolla FD, Jacobsen KW. Nature 1998;391:561–3.
[31] Meyers MA, Mishra A, Benson DJ. Prog Mater Sci 2006;51:427–556.
[32] Cheng S, Ma E, Wang Y, Kecskes L, Youssef K, Koch C, et al. Acta Mater 2005;53:1521–33.
[33] Chen J, Lu L, Lu K. Scripta Mater 2006;54:1913–8.
[34] Wang YM, Hamza AV, Ma E. Acta Mater 2006;54:2715–26.
[35] Schwaiger R, Moser B, Dao M, Chollacoop N, Suresh S. Acta Mater 2003;51:5159–72.
[36] Karanjgaokar NJ, Oh CS, Lambros J, Chasiotis I. Acta Mater 2012;60:5352–61.
[37] Gu P, Dao M, Asaro RJ, Suresh S. Acta Mater 2011;59:6861–8.
[38] Lu L, Zhu T, Shen Y, Dao M, Lu K, Suresh S. Acta Mater 2009;57:5165–73.
[39] Rinaldi A, Peralta P, Friesen C, Sieradzki K. Acta Mater 2008;56:511–7.
[40] Chen XX, Ngan AHW. Scripta Mater 2011;64:717–20.
[41] Alshehri O, Yavuz M, Tsui T. Acta Mater 2013;61:40–50.
[42] Jang D, Greer JR. Scripta Mater 2011;64:77–80.
[43] Greer JR, Oliver WC, Nix WD. Acta Mater 2005;53:1821–30.
[44] Zhang JY, Lei S, Niu J, Liu Y, Liu G, Zhang X, et al. Acta Mater 2012;60:4054–64.
[45] Zhang JY, Liu G, Lei SY, Niu JJ, Sun J. Acta Mater 2012;60:7183–96.
[46] Kiener D, Grosinger W, Dehm G. Scripta Mater 2009;60:148–51.
[47] Lee S-W, Han SM, Nix WD. Acta Mater 2009;57:4404–15.
[48] Han SM, Bozorg-Grayeli T, Groves JR, Nix WD. Scripta Mater 2010;63:1153–6.
[49] Sneddon IN. Int J Eng Sci 1965;3:47–57.
[50] Bharathula A, Lee SW, Wright WJ, Flores KM. Acta Mater 2010;58:5789–96.
[51] Xie KY, Shrestha S, Cao Y, Felfer PJ, Wang Y, Liao X, et al. Acta Mater 2013;61:439–52.
[52] Bei H, Shim S, Pharr GM, George EP. Acta Mater 2008;56:4762–70.
[53] Schneider AS, Kiener D, Yakacki CM, Maier HJ, Gruber PA, Tamura N, et al. Mater Sci Eng A 2013;559:147–58.
[54] Lu L, Schwaiger R, Shan ZW, Dao M, Lu K, Suresh S. Acta Mater 2005;53:2169–79.
[55] Han WZ, Demkowicz MJ, Fu EG, Wang YQ, Misra A. Acta Mater 2012;60:6341–51.
[56] Wu ZX, Zhang YW, Jhon MH, Greer JR, Srolovitz DJ. Acta Mater 2013;61:1831–42.
[57] Gu XW, Loynachan CN, Wu Z, Zhang YW, Srolovitz DJ, Greer JR. Nano Lett 2012;12:6385–92.
[58] Jang DC, Cai C, Greer JR. Nano Lett 2011;11:1743–6.
[59] Zerilli FJ, Armstrong RW. J Appl Phys 1987;61:1816.
[60] Kiener D, Guruprasad PJ, Keralavarma SM, Dehm G, Benzerga AA. Acta Mater 2011;59:3825–40.
[61] Dimiduk DM, Uchic MD, Parthasarathy TA. Acta Mater 2005;53:4065–77.
[62] Schiotz J, Jacobsen KW. Science 2003;301:1357–9.
[63] Lu L, Chen X, Huang X, Lu K. Science 2009;323:607–10.
[64] Shen YF, Lu L, Dao M, Suresh S. Scripta Mater 2006;55:319–22.
[65] Kiener D, Motz C, Rester M, Jenko M, Dehm G. Mater Sci Eng A 2007;459:262–72.
[66] Mayer J, Giannuzzi LA, Kamino T, Michael J. MRS Bull 2007;32:400.
[67] Shim S, Bei H, Miller MK, Pharr GM, George EP. Acta Mater 2009;57:503–10.
[68] Zimmermann J, Van Petegem S, Bei H, Grolimund D, George EP, Van Swygenhoven H. Scripta Mater 2010;62:746–9.
[69] Kiener D, Zhang Z, Sturm S, Cazottes S, Imrich PJ, Kirchlechner C, et al. Philos Mag 2012;92:3269–89.
[70] Bei H, Shim S, George EP, Miller MK, Herbert EG, Pharr GM. Scripta Mater 2007;57:397–400.
[71] Richter G, Hillerich K, Gianola DS, Monig R, Kraft O, Volkert CA. Nano Lett 2009;9:3048–52.
[72] Chisholm C, Bei H, Lowry MB, Oh J, Syed Asif SA, Warren OL, et al. Acta Mater 2012;60:2258–64.
[73] Zhang JY, Zhang X, Wang RH, Lei SY, Zhang P, Niu JJ, et al. Acta Mater 2011;59:7368–79.
[74] Arzt E, Dehm G, Gumbsch P, Kraft O, Weiss D. Prog Mater Sci 2001;46:283–307.
[75] Christian JW, Mahajan S. Prog Mater Sci 1995;39:1–157.
[76] Van Swygenhoven H, Derlet P, Froseth A. Acta Mater 2006;54:1975–83.
[77] Yamakov V, Wolf D, Phillpot SR, Mukherjee AK, Gleiter H. Nat Mater 2004;3:43–7.
[78] Zhang JY, Cui JC, Liu G, Sun J. Scripta Mater 2013;68:639–42.
[79] El-Awady JA, Rao SI, Woodward C, Dimiduk DM, Uchic MD. Int J Plasticity 2011;27:372–87.
[80] Zhou C, Beyerlein IJ, LeSar R. Acta Mater 2011;59:7673–82.
[81] Wei Q. J Mater Sci 2007;42:1709–27.
[82] Mompiou F, Caillard D, Legros M, Mughrabi H. Acta Mater 2012;60:3402–14.
[83] Li JCM, Chou YT. Metall Mater Trans B 1970;1:1145–59.
[84] Estrin Y, Kim HS, Nabarro FRN. Acta Mater 2007;55:6401–7.
[85] Nabarro FRN. Acta Metall Mater 1990;38:161–4.
[86] Dunstan DJ, Bushby AJ. Int J Plasticity 2013;40:152–62.
[87] Hartmaier A, Fivel MC, Canova GR, Grumbsch P. Model Simul Mater Sci Eng 1999;7:781.
[88] Świątnicki WA, Łojkowski W, Grabski MW. Acta Mater 1986;34:599–605.
[89] Zhu T, Li J. Prog Mater Sci 2010;55:710–57.
[90] Suresh S, Li J. Nature 2008;456:716–7.